nature materials

Article

https://doi.org/10.1038/s41563-022-01449-1

Tunable photon-induced spatial modulation of free electrons

Received: 7 October 2021

Accepted: 26 November 2022

Published online: 26 January 2023

Check for updates

Shai Tsesses[1,4], Raphael Dahan[1,2,4], Kangpeng Wang[1,2,3], Tomer Bucher[1,2], Kobi Cohen[1], Ori Reinhardt[1,2], Guy Bartal[1] & Ido Kaminer[1,2]

Spatial modulation of electron beams is an essential tool for various applications such as nanolithography and imaging, yet its conventional implementations are severely limited and inherently non-tunable. Conversely, proposals of light-driven electron spatial modulation promise tunable electron wavefront shaping, for example, using the mechanism of photon-induced near-field electron microscopy. Here we present tunable photon-induced spatial modulation of electrons through their interaction with externally controlled surface plasmon polaritons (SPPs). Using recently developed methods of shaping SPP patterns, we demonstrate a dynamic control of the electron beam with a variety of electron distributions and verify their coherence through electron diffraction. Finally, the nonlinearity stemming from energy post-selection provides us with another avenue for controlling the electron shape, generating electron features far below the SPP wavelength. Our work paves the way to on-demand electron wavefront shaping at ultrafast timescales, with prospects for aberration correction, nanofabrication and material characterization.

Current technologies for spatial modulation of coherent electron beams are based on three enabling technologies: tailored electro- and magneto-static fields[1,2], applying force to change electron trajectories; apertures[3] or binary holograms[4], nullifying electron transmission at pre-selected locations; and electron phase plates[5] or holograms[6–9], utilizing variations in thin-film thickness to shape the phase-front of the electron beam. Nevertheless, most contemporary methods lack the means to actively change the electron beam shape. Even state-of-the-art electron beam shaping technologies[10–12]—able to dynamically shift electron patterns in continuous beam operation—are still restricted in their tunability, operation speed and scalability. Since spatial modulation of electron beams is required for various uses[13–15], and tunable spatial modulation has already revolutionized the fields of optics[16] and acoustics[17], breakthroughs advancing this enabling technology in electron optics are expected to facilitate potential discoveries and promote future applications.

A promising new approach to spatially modulate electrons relies on an entirely different physical mechanism—the interaction of free electrons with light, either in the presence of nanophotonic platforms[18–21] or through the ponderomotive force in free space[22,23]. Such an interaction produced basic electron patterns in the image or diffraction plane of an electron microscope[18–20,22], inspiring several theoretical proposals[24–26] for the design of a nearly arbitrary, light-driven electron spatial modulator. This concept, however, has never been demonstrated experimentally.

Our work takes the next step in this direction, displaying complex electron patterns and demonstrating control over them by tuning external light properties and by post-selecting electrons in different energy ranges. The demonstrated light-driven electron distributions include various Bessel beams and vortex arrays, generated using a patterned gold-coated silicon nitride membrane placed inside an ultrafast transmission electron microscope (UTEM). Furthermore, we verify the coherence of our spatial modulation scheme by demonstrating electron diffraction off of a standing wave of surface plasmon polaritons (SPPs), which is a plasmonic analogue of the Kapitza–Dirac effect[27].

[1]Andrew and Erna Viterbi Department of Electrical Engineering, Technion, Israel Institute of Technology, Haifa, Israel. [2]Solid State Institute, Technion, Israel Institute of Technology, Haifa, Israel. [3]Shanghai Institute of Optics and Fine Mechanics, Chinese Academy of Sciences, Shanghai, China. [4]These authors contributed equally: Shai Tsesses, Raphael Dahan. e-mail: kaminer@technion.ac.il

We then continuously tune the shape of an electron in a superposition of Bessel modes, showcasing the potential to adjust the orbital angular momentum of electrons in real time. By post-selecting specific electron energies after their interaction with the guided SPPs in our sample, we unlock another type of electron spatial modulation, obtained by adjusting the incident laser intensity and pulse width. Our findings have an impact on state-of-the-art electron imaging and characterization techniques, taking a step towards fully programmable electron beams, whose applications range from adaptive aberration correction in electron microscopes to on-demand generation of masks for electron beam lithography.

Theory and experimental apparatus

Our scheme is based on the interaction of paraxial electron pulses with ultrafast SPP fields, which can be described by the following equation[28–30]:

$$\left[U_0 - \hbar v\left(i\frac{\partial}{\partial z} + k_0\right) - \frac{ie\hbar}{\omega}\left(E_z(x,y,z,t)\exp(-i\omega t)\right.\right.$$
$$\left.\left.-E_z^*(x,y,z,t)\exp(i\omega t)\right)\right]\psi = i\hbar\frac{\partial\psi}{\partial t} \quad (1)$$

where v is the electron velocity; k_0 is the initial electron wave-vector; U_0 is the initial electron energy; E_z and E_z^* are the SPP electric field phasor in the direction of electron propagation and its complex conjugate, respectively; ω is the central frequency of the SPP field; e is the electron charge; $\hbar$ is the reduced Planck constant; t is time; and ψ is the electron wavefunction.

Equation (1) shows that the electron wavefunction is only influenced by the shape of the z component of the electric field, E_z, due to the large electron momentum in the propagation direction, which also makes the scalar potential and ponderomotive force contributions negligible. To solve equation (1), it is customary to neglect the electron recoil in the interaction[28–30] and assume that the SPP field has a slowly varying temporal envelope[31]. Then, the electric field acts on the electron wavefunction in a similar manner to a phase mask[30,32]:

$$\psi = \psi_0 \sum_{l=-\infty}^{\infty} J_l(2|g(x,y)|)\exp(il\arg(-g(x,y)))\exp\left(il\omega\left(\frac{z}{v}-t\right)\right)$$
$$= \psi_0 \exp(2i|g(x,y)|\sin\left(\omega\left(t-\frac{z}{v}\right)-\arg(g(x,y))\right)) \quad (2)$$

where ψ_0 is the initial electron wavefunction; J_l is the lth order Bessel function of the first kind, with l denoting the interaction order that is summed over; and $g(x,y) = \frac{e}{\hbar\omega}\int_{-\infty}^{\infty}E_z(x,y,z)\exp(-i\frac{\omega}{v}z)dz$ is the free-electron–light interaction strength, containing the transverse (x,y) spatial dependence of the modulation.

Equation (2) indicates that the probability P_l of the electron in point (x,y) to absorb or emit l photons is

$$P_l(x,y) \propto J_l^2(2|g(x,y)|). \quad (3)$$

By post-selecting electrons of a specific energy range, one can isolate a specific interaction order or several of them. Then, regardless of the interaction strength, the modulation is no longer confined to the electron phase but involves its amplitude as well. An illustration of this spatial modulation concept is given in Fig. 1.

The electron wavefunction dependence on the parameter g defines two regimes of free-electron–light interaction: a low-intensity and a high-intensity regime. The low-intensity regime is achieved when $g \ll 1$ or when the laser pulse duration is much shorter than the electron pulse (further details in Methods). In this regime, the electron probability distribution for gaining energy roughly scales as[28,29] $P_{l>0}(x,y) \propto |g(x,y)|^2 \propto |E_z(x,y)|^2$. The low-intensity regime has been used in most photon-induced near-field electron microscopy (PINEM) experiments thus far[18,19,31,33–37], and the spatial modulation it enforces on the electron is directly derived from the shape of the electromagnetic near field, such as the one obtained by SPPs. By contrast, stronger laser intensities ($g \geq 1$), with a pulse duration longer than that of the electron, bring about the high-intensity regime[20,31,35,38–40]. In this regime, the shape of electrons in each interaction order l is unique and can differ greatly from the shape of the electric field (the wavefunction of each interaction order depends nonlinearly on the field).

For both interaction regimes, we shape long-range SPPs in a thin gold-coated silicon nitride membrane using specially designed coupling slits[41–43] (Fig. 2e,f). The coupling slits enable dynamic control over the electron wavefunction by altering the SPP field through the incident illumination (amplitude and polarization). We use weakly focused femtosecond laser pulses that impinge on the coupling slits inside a UTEM (Fig. 2a, Extended Data Fig. 1 and Methods contain further details about the sample, its optical properties and the experimental system). Femtosecond free-electron pulses arrive at the coupling slit simultaneously with the laser pulses and pass through their unpatterned central area. Thus, the entire electron shaping is produced by the SPP field at the centre without any contribution from the coupling slits. The resulting shaped electron distribution, both amplitude and phase, is thus achieved at the image plane of the membrane (rather than at the diffraction plane as in most other methods).

Spatial modulation in the low-intensity regime

We first present spatial electron modulation in the low-intensity regime. We filter the energy of post-interaction electrons with a wide window at the gain side of the electron energy spectrum, effectively collecting the signal from all electrons that gained energy ($l > 0$). The results are summarized in Fig. 2b–g, presenting various examples of electron spatial modulation enabled by shaping the SPPs: a first-order Bessel electron vortex (Fig. 2b); a hexagonal electron vortex array (Fig. 2c); and a hexagonal foci array (Fig. 2d), generated by shifting one edge of the coupling slit used in Fig. 2c.

Each measurement is accompanied by the calculated electron probability distribution after interaction with the out-of-plane SPP field of the sample (Fig. 2h–j), showing a good match between experiment and theory (full calculation details and the procedure for processing the raw electron microscope images are given in Methods). Though the total SPP field producing each of these electron distributions has in-plane components as well[44,45], they do not contribute to the electron distribution.

We note that our photon-induced spatial modulation matches state-of-the-art passive electron spatial modulation schemes in quality[46,47], while going beyond the single, localized vortex previously generated through free-electron–light interactions[19]. Importantly, the hexagonal electron foci lattice is generated by a lattice of SPP skyrmions in the electric field[48–51], whose influence on the amplitude of an incident electron beam is surprisingly similar to their magnetic counterparts' influence on the beam's phase[52].

We next employ electron diffraction to show that our photon-induced shaped electrons have transverse coherence (as is customary in the field of coherent electron shaping[53]). Figure 3a–e shows the diffraction of electrons due to their interaction with a hexagonal SPP vortex array (Fig. 2c), where we capture and isolate diffraction stemming solely from SPPs. Incidentally, to the best of our knowledge, this is the first measurement of electron diffraction from standing-wave SPPs, which was predicted by ref. [27]. Contrarily, past experiments measuring electron diffraction by light relied on the electrons interacting with the direct laser illumination (as in Fig. 3f–j). The laser creating the diffraction in such cases was either reflected by a mirror[20,35] or scattered by a nanoscale pattern[19] for interaction with near fields, or it interacted with the electrons directly via the ponderomotive force[22,23,54]. Our experiment demonstrates diffraction not by direct laser illumination but by the long-range SPPs excited at the surface, thus illustrating the transverse coherence of electrons shaped by the patterned near field.

https://doi.org/10.1038/s41563-022-01449-1

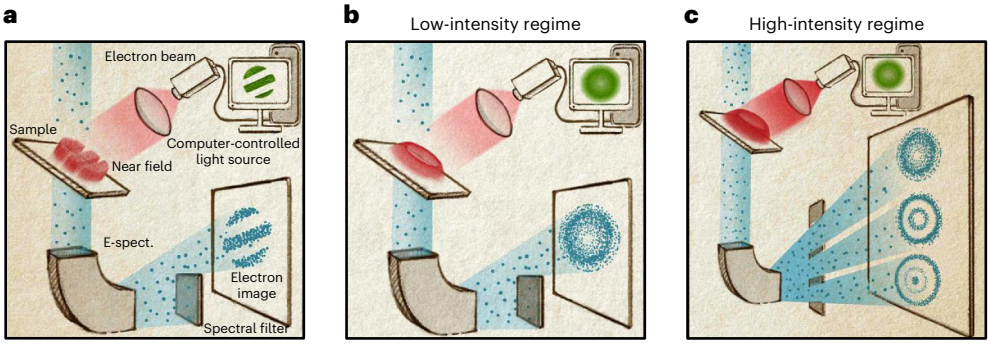

Fig. 1 | Concept illustration of tunable photo-induced free-electron spatial amplitude modulation. a, In a similar fashion to PINEM experiments[31,33,34,36,38], a laser excitation (red) is used to create a specific near-field distribution. The required laser illumination can be controlled automatically by external software. An electron beam (blue) interacts with the near field and is shaped by it. After propagating through various electron optical components (not shown), the electron beam enters an electron energy spectrometer (E-spect.) that post-selects certain electron energies with a spectral filter. The selected electrons are then imaged by a camera, revealing that they now possess the near-field shape, or a nonlinear function of it. **b**, In the low-intensity regime of the free-electron–light interaction, post-selecting all electrons that gained energy imprints the near-field spatial distribution directly on the electron beam. **c**, In the high-intensity regime of the free-electron–light interaction, post-selecting specific electron energies imprints different spatial shapes on the electrons, each energy having a different nonlinear dependence on the near-field amplitude (larger power is depicted by a darker red colour). Thus, both the shape of the near field (in the low-intensity regime) and its amplitude (in the high-intensity regime) are tunable degrees of freedom with which we can spatially modulate electron beams. Drawings were produced by SimplySci.

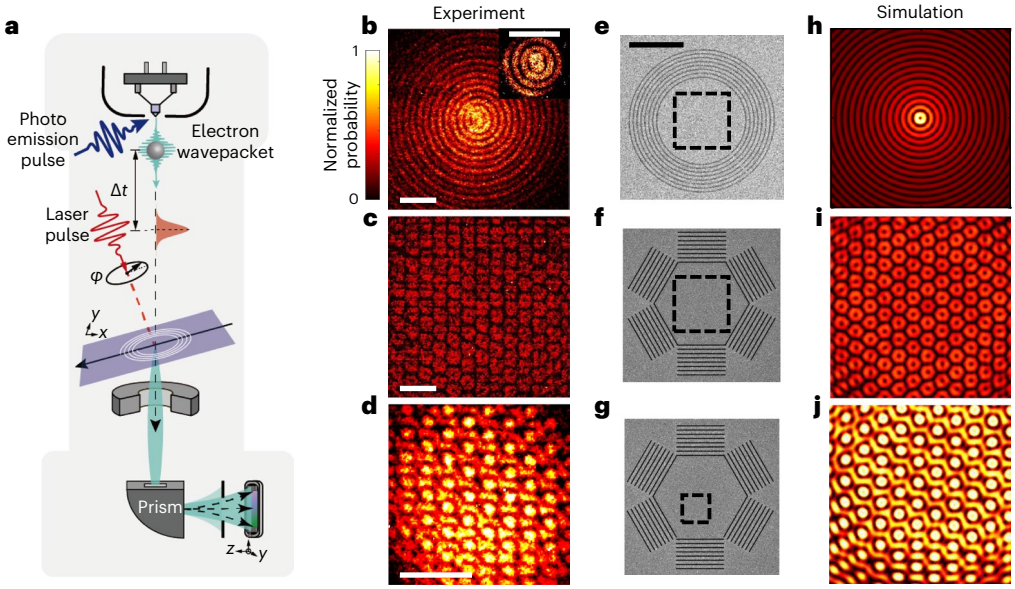

Fig. 2 | Experimental set-up and proof of concept of photon-induced spatial modulation of free electrons. a, An illustration of the UTEM. After interaction with the generated near field in the sample, which is controlled by the incident laser polarization φ, the electrons are imaged at the output plane of the membrane. The electron signal is post-selected using energy-filtered imaging to show the distribution of electrons at specific energy ranges. The turquoise pulse represents the electron wavepacket, while red and blue pulses represent the laser pulses generating the near field and the electron photoemission, respectively. **b**–**j**, Measured electron probability distributions after interaction with the near field of various plasmonic patterns (**b**–**d**). The patterns shown here were generated using circularly polarized illumination of coupling slits with different geometries (**e**–**g**), including a first-order Bessel electron vortex (**b**), a hexagonal electron vortex array (**c**) and a hexagonal electron foci array (**d**). Each measured electron distribution in **b**–**d** is complemented by the corresponding calculated probability distributions (**h**–**j**), showing a good match between theory and experiments. The electron distribution follows the shape of the plasmonic near field as expected in the low-intensity interaction regime. The measurement areas in **b**–**d** are marked by dashed squares in **e**–**g**. The slit in **g** differs from **f** only by a shift of the bottom coupling grating by half the plasmonic wavelength, thus exciting a foci array instead of a vortex array. The inset in **b** shows a larger magnification image of the measured distribution, where the vortex singularity is more clearly visible. The black scale bar in **e** (relevant to **f** and **g** as well) corresponds to 10 µm. All white scale bars in **b**–**d** correspond to 2 µm. The colour bar in **b**, relevant to **b**–**d** and **h**–**j**, represents the normalized probability distribution of the electron.

Figure 3b,c confirms that the diffracted electrons gain exactly the transverse momentum embedded in the plasmonic lattice, and further includes a signature of second-order diffraction by combinations of pairs of plasmonic lattice momenta. By comparison, we also record the diffraction from the localized electric near field directly inside and around the coupling slits (Fig. 3g,h). Higher order diffraction is visible there (along the outer white rings) but always limited to multiples of individual plasmonic lattice momenta, rather than

https://doi.org/10.1038/s41563-022-01449-1

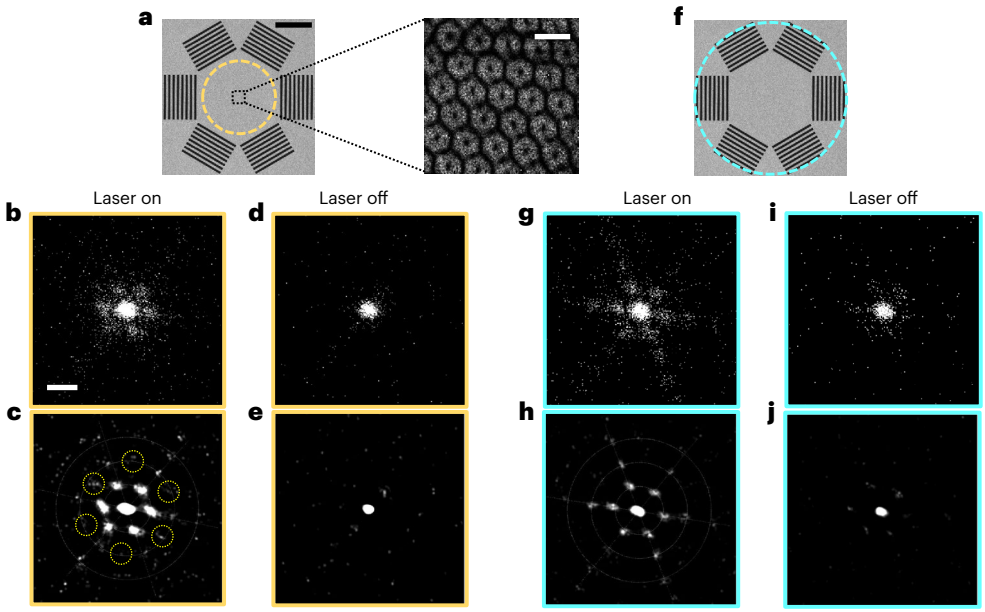

Fig. 3 | Electron diffraction from a hexagonal plasmonic vortex array. a, An SEM micrograph of the plasmonic coupling slit. Marked within it is the aperture used to truncate the electron beam such that it interacts only with the plasmonic pattern and not with the coupling slit (dashed gold circle). The zoomed-in inset (dotted black square) presents the electron distribution at the centre of the slit, which is similar to Fig. 2c. White and black scale bars are 1 and 10 µm, respectively. **b**–**e**, Drift-corrected diffraction images, organized as follows: diffraction with illumination (laser on; **b**,**c**) and without illumination (laser off; **d**,**e**) is given in two separate columns, while the original (**b**,**d**) and deconvolved (**c**,**e**) images are placed in two separate rows. The thin white lines and circles in **c** mark the angles of the six SPP wavevectors and corresponding multiples of the SPP wavenumber. The white scale bar in **b**, relevant for all diffraction images, is 10 reciprocal micrometres. All diffraction images include no energy filtering. **f**–**j**, The same items as **a**–**e** but with a larger aperture used to truncate the electron beam, such that it covers the coupling slit (dashed turquoise circle in **f**). The diffraction signal in **g**–**j** is dominated by electrons passing through the coupling slit. It includes inelastic scattering that is not induced by light (**i**,**j**) and is mainly affected by the localized near field inside and around the slits as it cannot create second-order diffraction peaks that combine two different components of the plasmonic lattice momenta. By contrast, the second-order peaks marked by yellow dotted circles in **c** arise from electron interaction with the plasmonic pattern—the interference of multiple plasmonic lattice momenta. The diffraction measurements attest to the transverse coherence of the electrons after their shaping by the SPP near field.

combinations of different pairs (marked in Fig. 3c; absent in Fig. 3h). Different pair combinations are only possible when the diffraction is from the interference of propagating SPPs, forming a standing wave at the centre of the sample.

After establishing the variety and quality of electron spatial modulation possible using our scheme, we demonstrate its tunability via external control of the near-field profile (Fig. 4). Using a spiral plasmonic coupling slit, we alter the boundary conditions of the SPP field as a function of the polarization of the incident laser pulse, which then determines the interference pattern within the slit. The gradual change of the laser polarization results in the excitation of either one of two specific Bessel modes[42] or their superposition[55], which is imprinted on the electron (Supplementary Videos 1 and 2). Slight distortions in the shape of the modes arise from the nonideal nature of the spiral slit excitation and the impurity of the polarization in our system.

Spatial modulation in the high-intensity regime

We next demonstrate spatial electron modulation in the high-intensity regime of the free-electron–light interaction. While the low-intensity regime allows direct imprinting of the amplitude of the near field onto the electron wavefunction, the high-intensity regime provides a unique degree of freedom for electron beam shaping arising from the possibility of energy post-selection. Energy post-selection can create an inherently nonlinear connection between the SPP pattern and the electron distribution, as is evident in equation (3). This nonlinear connection does not exist in other electron-shaping methods, and it enables more complex spatial modulation schemes. We note that in completely different fields, the creation of nonlinearity using post-selection is a well-known concept, for example, in measurement-based quantum computation[56].

Figure 5 demonstrates the nonlinear connection between the SPP pattern and the resulting post-selected electron distribution. We use the same circular coupling slit and incident polarization as in Fig. 2b, while increasing both the power and temporal duration of the incident laser pulses. Figure 5a,b presents the measured probability distribution in each non-negative interaction order $l = 0$–5 for two different laser powers (more details on the experimental parameters appear in Methods and Extended Data Fig. 2). The shape of each interaction order l is governed by an interplay between its distribution function (lth order Bessel function of the first kind) and the spatial dependence of its argument $(2|g(x,y)|)$, as seen in equation (3). This nonlinear connection can be used as a tool for spatially modulating electrons by altering either the impinging laser power or the filtered electron energy. The interaction orders $l = 2$ in Fig. 5a and $l = 4$ in Fig. 5b are a clear demonstration of this mechanism, as they present a similar distribution in different interaction orders, brought on solely by changing the excitation laser pulse energy.

To compare the low-intensity and high-intensity regimes of free-electron–light interactions, Fig. 5c presents the electron distribution in the low-intensity regime, after collecting the signal from all electrons that gained energy ($l > 0$; that is, summing over all positive interaction orders). As expected, the distribution is similar to the SPP pattern, a first-order Bessel function of the first kind. By contrast, part of the distributions in Fig. 5a,b (especially $l = 1, 2$ in Fig. 5a and $l = 1$–5 in Fig. 5b) substantially differ from the SPP pattern. This comparison is quantified in Fig. 5d, presenting a radial average showing the similarity of the distribution in Fig. 5c to the theoretical distribution of the SPP pattern and its difference from the distributions of $l = 0, 2$ in Fig. 5a. Further away from the slit's centre, the electron distribution

https://doi.org/10.1038/s41563-022-01449-1

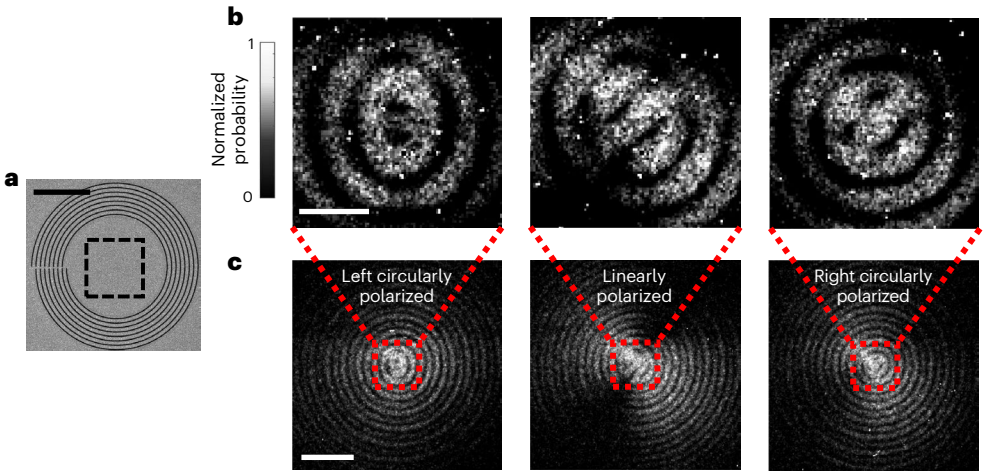

Fig. 4 | Spatial modulation of free electrons by active control of SPP boundary conditions. a, An SEM micrograph of the spiral coupling slit used for the measurements, with the measurement area marked by a dashed square. Scale bar, 10 µm. **b**, Measured normalized probability distribution of gain-filtered electrons ($l > 0$) as a function of the rotation angle of a quarter-wave plate placed outside the UTEM, which controls the laser pulse polarization. As the quarter-wave plate rotates, the electron gradually transforms from a second-order Bessel mode to a zero-order Bessel mode, existing in a superposition of both modes at any intermediate step. Scale bar, 0.5 µm. **c**, Corresponding lower magnification images of the electron distribution, with the incident polarization created by the quarter-wave plate rotation written in every panel. Scale bar, 2.5 µm. The colour bar in **b**, relevant for **c** as well, represents the normalized electron probability distribution. The complete dataset with additional rotation angles of the quarter-wave plate is presented in Supplementary Videos 1 and 2.

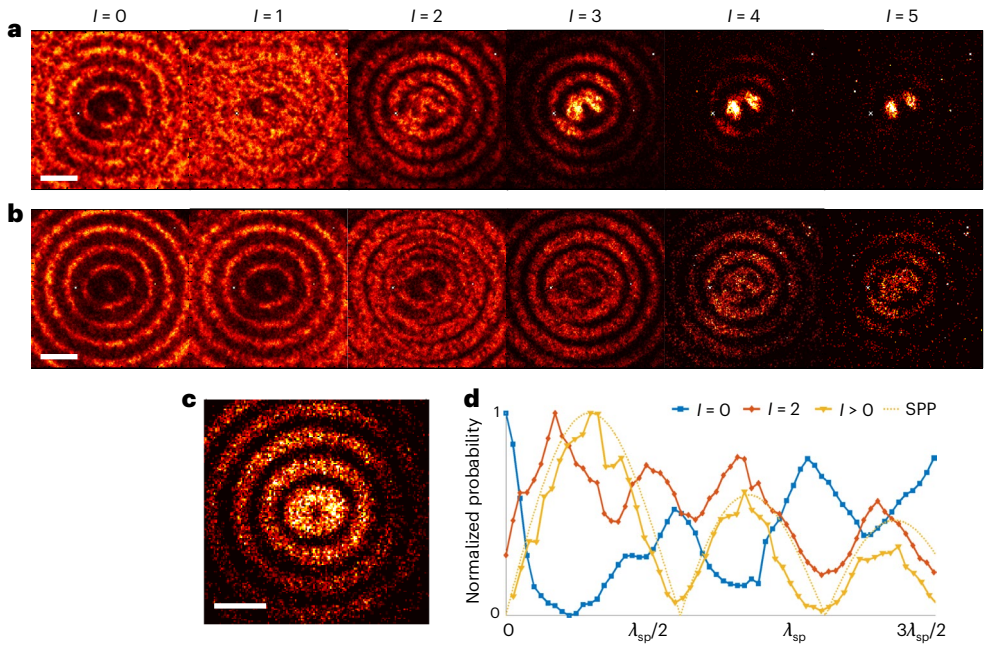

Fig. 5 | Nonlinear control over the electron distribution using a plasmonic pattern and electron post-selection. a,**b**, Demonstration of the high-intensity regime of free-electron–light interaction. Electron distributions for interaction orders $l = 0$–5 and laser pulse energies 30 nJ (**a**) and 65 nJ (**b**). The laser pulse duration is 2.4 times longer than the electron pulse, guaranteeing an approximately uniform intensity throughout the interaction. **c**, Comparison with the low-intensity regime of the free-electron–light interaction. The electron distribution is created by combining all positive interaction orders, using a laser pulse of 25 nJ energy and a duration 1.6 times shorter than the electron pulse. This electron distribution resembles the plasmonic pattern, a first-order Bessel function of the first kind. The individual interaction orders in **a** and **b** are post-selected by EFTEM using a sharp energy filter of 1 eV, centred about the energy of each interaction order ($l \times 1.7$ eV). By comparison, the energy filter in **c** is wide enough to include all electrons gaining energy in the interaction (10-eV-wide slit centred at 6 eV). All white scale bars correspond to one plasmonic wavelength. The $l = 0$ interaction order in **a** and **b** presents a central spot with a full-width at half-maximum (FWHM) of ~140 nm and ~70 nm, which are a fifth and a tenth of the plasmonic wavelength λ_{sp}, respectively. **d**, The radial average of **c** (labelled '$l > 0$') resembles the SPP distribution (labelled 'SPP'), as expected in the low-intensity regime. By contrast, the radial average of electrons of individual interaction orders (showing $l = 0, 2$) in the high-intensity regime in **a** show distinctly different patterns. The incident polarization and coupling slit used are the same as in Fig. 2b.

gradually resembles a power of the SPP pattern, since the SPP amplitude decreases. At each interaction order, this phenomenon becomes apparent at a larger distance for increased laser pulse energy.

The high-intensity regime enables the generation of feature sizes in the electron distribution that are far smaller than those in the near field, by exploiting the nonlinear connection between them.

A prominent example of a deep-subwavelength feature is apparent as an oval spot at the centre of the $l = 0$ interaction order in Fig. 5a,b (that is, electrons gaining no energy in the interaction), which can be compared with the near-field distribution in Fig. 5d. This feature is an order of magnitude smaller than the plasmonic wavelength λ_{sp} (in Fig. 5b). The feature is generated by the phase singularity at the centre of the Bessel vortex near field, which allows electrons to pass without interaction in an area whose size decreases for a larger near-field amplitude. Such a phenomenon is brought on by the nonlinear functional dependence of the post-selected electrons, similar to the mechanism of stimulated emission depletion currently used in super-resolution fluorescence microscopy[57].

Intriguingly, our results in Fig. 5 show an effect known as free-electron Rabi oscillations. This effect was first observed and named by ref. [39] as the oscillations in the energy-level occupations of the electron as a function of the field intensity. This phenomenon was previously demonstrated using electron energy loss spectroscopy (EELS) with a focused electron beam, either interacting with a near field at a certain position[39] or scanned over a near-field distribution[31,38]. In contrast with these previous works, and similarly to some results by ref. [40], we measured this phenomenon in energy-filtered transmission electron microscopy (EFTEM). This way, each measurement captures the entire electron pattern, and the Rabi oscillations are revealed by scanning over the energy filter instead. Considering this result together with the transverse coherence demonstrated in Fig. 3, we can conclude that the probability of the electron to occupy different energy levels oscillates coherently and in various positions simultaneously.

Discussion and outlook

In conclusion, we demonstrated both passive and active photon-induced spatial electron modulation. The experiments rely on the interactions of free-electron pulses with ultrafast SPP excitations in a metal–dielectric membrane. Our approach promises more degrees of freedom for active spatial modulation, simpler fabrication than other current methods and operation at ultrafast timescales—a step towards complete spatiotemporal modulation of electron wavefunctions[26]. Furthermore, our scheme is freely available to use in any ultrafast electron microscope or in other electron microscope variants capable of optically modulating electrons[58,59], as it requires only standard fabrication processes, optical components and electron optics.

Similarly to other electron-shaping methods[53], focusing the electrons is required after the shaping to reach feature sizes at the electron resolution limit. In addition, using a brighter electron source and better electron optics, as in the work of ref. [20], can improve the acquisition speeds of electron distribution in the image and diffraction planes, which were limited here to several minutes and several hours, respectively (more details in Methods).

It is interesting to compare the prospects of electron beam shaping via PINEM[28,29,33], as demonstrated here, to other experiments involving free-electron–light interactions, such as two-photon photoemission electron microscopy (2PPE-PEEM)[49,60–63]. Some 2PPE-PEEM experiments imaged SPP patterns resembling Fig. 4 and controlled them by altering the incident laser polarization[64]. However, in contrast with PINEM[18–20] and ponderomotive schemes[22,23,65], the control of electron distributions in 2PPE-PEEM is via photoemission, which may impair the transverse electron coherence[66]. Interestingly, 2PPE-PEEM and other methods[67] can sense the vectorial nature of the near field, an ability only theoretically considered for PINEM thus far[31], which could add additional degrees of freedom to control electron wavefunctions.

Superficially, tunable spatial electron modulation may seem analogous to the way spatial light modulators shape light. However, the mechanism of our spatial modulation scheme is actually analogous to acousto-optical deflection[68], which is also commonly used for shaping beams of light[69]. Importantly, energy post-selection allows the near field to directly modulate both the phase and amplitude of free electrons, as evidenced by our electron diffraction measurements and also shown theoretically in Extended Data Fig. 3. Intriguingly, our results imply that using a plasmonic vortex for shaping in the high-intensity regime creates an electron distribution containing different angular momenta for different interaction orders, as predicted by ref. [32], making the angular momentum of the entire electron wavefunction spatially dependent.

Considering all the above, the electron-shaping platform presented herein has the potential to immediately impact state-of-the-art electron imaging and characterization techniques. For example, a continuous and/or ultrafast tuning of an electron beam's angular momentum could enable characterization of chiral and magnetic materials[46] with high temporal and spatial resolutions. We also envision the generation of tunable nanometric apertures, smaller than those currently used in electron microscopes, in which electrons can pass freely only in certain areas defined by a predesigned laser intensity pattern (as in Fig. 5). Furthermore, by matching an electron beam pattern to a desired lattice shape or symmetry (as in Fig. 2c,d), electrons can be made to pass through the crystal with reduced scattering or to excite only specific atoms in heterogeneous crystals.

Looking forward, our demonstration of tunable spatial modulation is a step towards fully programmable electron beams with arbitrarily controllable wavefronts, which has yet to be achieved. Further improvements can be made by using a spatial light modulator[70] to shape the incoming laser pulses, or employing multiple confined surface modes as in a multimode planar waveguide, potentially using multi-frequency illumination[30]. In the end, complete automation of the photon-induced spatial modulation process promises real-time optimization of electron beam shapes for continuous aberration correction of electron beams, on-demand generation of patterns for electron beam lithography and electron beam focusing inside samples beyond the mean free path restriction.

Online content

Any methods, additional references, Nature Portfolio reporting summaries, source data, extended data, supplementary information, acknowledgements, peer review information; details of author contributions and competing interests; and statements of data and code availability are available at https://doi.org/10.1038/s41563-022-01449-1.

References

1. Hawkes, P. W. & Kasper, E. in *Principles of Electron Optics* Vol. 1 (eds Hawkes, P. W. & Kasper, E.) 276–289 (Academic Press, 1996).
2. Haider, M. et al. Electron microscopy image enhanced. *Nature* **392**, 768–769 (1998).
3. Jönsson, C. Elektroneninterferenzen an mehreren künstlich hergestellten feinspalten. *Z. Phys.* **161**, 454–474 (1961).
4. Verbeeck, J., Tian, H. & Schattschneider, P. Production and application of electron vortex beams. *Nature* **467**, 301–304 (2010).
5. Uchida, M. & Tonomura, A. Generation of electron beams carrying orbital angular momentum. *Nature* **464**, 737–739 (2010).
6. McMorran, B. J. et al. Electron vortex beams with high quanta of orbital angular momentum. *Science* **331**, 192–195 (2011).
7. Grillo, V. et al. Generation of nondiffracting electron bessel beams. *Phys. Rev. X* **4**, 011013 (2014).
8. Shiloh, R., Lereah, Y., Lilach, Y. & Arie, A. Sculpturing the electron wave function using nanoscale phase masks. *Ultramicroscopy* **144**, 26–31 (2014).
9. Harvey, T. R. et al. Efficient diffractive phase optics for electrons. *New J. Phys.* **16**, 93039 (2014).
10. Verbeeck, J. et al. Demonstration of a 2 × 2 programmable phase plate for electrons. *Ultramicroscopy* **190**, 58–65 (2018).

11. Tavabi, A. H. et al. Experimental demonstration of an electrostatic orbital angular momentum sorter for electron beams. *Phys. Rev. Lett.* **126**, 94802 (2021).
12. Verbeeck, J., Ibáñez, F. V. & Béché, A. Demonstration of a 48 pixel programmable phase plate for adaptive electron optics. In *Proc. Electron Beam Spectroscopy for Nanooptics* (nanoGe, 2021).
13. Vieu, C. et al. Electron beam lithography: resolution limits and applications. *Appl. Surf. Sci.* **164**, 111–117 (2000).
14. Adrian, M., Dubochet, J., Lepault, J. & McDowall, A. W. Cryo-electron microscopy of viruses. *Nature* **308**, 32–36 (1984).
15. Guzzinati, G. et al. Probing the symmetry of the potential of localized surface plasmon resonances with phase-shaped electron beams. *Nat. Commun.* **8**, 14999 (2017).
16. Grier, D. G. A revolution in optical manipulation. *Nature* **424**, 810–816 (2003).
17. Fink, M. Time reversal of ultrasonic fields. I: Basic principles. *IEEE Trans. Ultrason. Ferroelectr. Freq. Control* **39**, 555–566 (1992).
18. Madan, I. et al. Holographic imaging of electromagnetic fields via electron-light quantum interference. *Sci. Adv.* **5**, aav8358 (2019).
19. Vanacore, G. M. et al. Ultrafast generation and control of an electron vortex beam via chiral plasmonic near fields. *Nat. Mater.* **18**, 573–579 (2019).
20. Feist, A., Yalunin, S. V., Schäfer, S. & Ropers, C. High-purity free-electron momentum states prepared by three-dimensional optical phase modulation. *Phys. Rev. Res.* **2**, 043227 (2020).
21. Tsesses, S. et al. Spatial modulation of free-electron wavepackets by shaping ultrafast plasmonic excitations. In *Proc. 2020 Conference on Lasers and Electro-Optics (CLEO)* 1–2 (IEEE, 2020).
22. Schwartz, O. et al. Laser phase plate for transmission electron microscopy. *Nat. Methods* **16**, 1016–1020 (2019).
23. Mihaila, M. C. C. et al. Transverse electron beam shaping with light. *Phys. Rev. X* **12**, 031043 (2022).
24. Konečná, A. & de Abajo, F. J. G. Electron beam aberration correction using optical near fields. *Phys. Rev. Lett.* **125**, 30801 (2020).
25. de Abajo, F. J. G. & Konečná, A. Optical modulation of electron beams in free space. *Phys. Rev. Lett.* **126**, 123901 (2021).
26. Vanacore, G. M., Madan, I. & Carbone, F. Spatio-temporal shaping of a free-electron wave function via coherent light–electron interaction. *Riv. Nuovo Cim.* **43**, 567–597 (2020).
27. García De Abajo, F. J., Barwick, B. & Carbone, F. Electron diffraction by plasmon waves. *Phys. Rev. B* **94**, 041404(R) (2016).
28. Garcia De Abajo, F. J., Asenjo-Garcia, A. & Kociak, M. Multiphoton absorption and emission by interaction of swift electrons with evanescent light fields. *Nano Lett.* **10**, 1859–1863 (2010).
29. Park, S. T., Lin, M. & Zewail, A. H. Photon-induced near-field electron microscopy (PINEM): theoretical and experimental. *New J. Phys.* **12**, 123028 (2010).
30. Reinhardt, O. & Kaminer, I. Theory of shaping electron wavepackets with light. *ACS Photon.* **7**, 2859–2870 (2020).
31. Wang, K. et al. Coherent interaction between free electrons and a photonic cavity. *Nature* **582**, 50–54 (2020).
32. Cai, W., Reinhardt, O., Kaminer, I. & de Abajo, F. J. G. Efficient orbital angular momentum transfer between plasmons and free electrons. *Phys. Rev. B* **98**, 45424 (2018).
33. Barwick, B., Flannigan, D. J. & Zewail, A. H. Photon-induced near-field electron microscopy. *Nature* **462**, 902–906 (2009).
34. Piazza, L. et al. Simultaneous observation of the quantization and the interference pattern of a plasmonic near-field. *Nat. Commun.* **6**, 6407 (2015).
35. Vanacore, G. M. et al. Attosecond coherent control of free-electron wave functions using semi-infinite light fields. *Nat. Commun.* **9**, 2694 (2018).
36. Pomarico, E. et al. meV resolution in laser-assisted energy-filtered transmission electron microscopy. *ACS Photon.* **5**, 759–764 (2018).
37. Liu, H. et al. Visualization of plasmonic couplings using ultrafast electron microscopy. *Nano Lett.* **21**, 5842–5849 (2021).
38. Kfir, O. et al. Controlling free electrons with optical whispering-gallery modes. *Nature* **582**, 46–49 (2020).
39. Feist, A. et al. Quantum coherent optical phase modulation in an ultrafast transmission electron microscope. *Nature* **521**, 200–203 (2015).
40. Henke, J.-W. et al. Integrated photonics enables continuous-beam electron phase modulation. *Nature* **600**, 653–658 (2021).
41. Liu, Z. et al. Focusing surface plasmons with a plasmonic lens. *Nano Lett.* **5**, 1726–1729 (2005).
42. Gorodetski, Y., Niv, A., Kleiner, V. & Hasman, E. Observation of the spin-based plasmonic effect in nanoscale structures. *Phys. Rev. Lett.* **101**, 043903 (2008).
43. Liu, Z. et al. Broad band two-dimensional manipulation of surface plasmons. *Nano Lett.* **9**, 462–466 (2009).
44. Tsesses, S., Cohen, K., Ostrovsky, E., Gjonaj, B. & Bartal, G. Spin–orbit interaction of light in plasmonic lattices. *Nano Lett.* **19**, 4010–4016 (2019).
45. Frischwasser, K. et al. Real-time sub-wavelength imaging of surface waves with nonlinear near-field optical microscopy. *Nat. Photon.* **15**, 442–448 (2021).
46. Bliokh, K. Y. et al. Theory and applications of free-electron vortex states. *Phys. Rep.* **690**, 1–70 (2017).
47. Tavabi, A. H. et al. Generation of electron vortices using nonexact electric fields. *Phys. Rev. Res.* **2**, 013185 (2020).
48. Tsesses, S. et al. Optical skyrmion lattice in evanescent electromagnetic fields. *Science* **361**, 993–996 (2018).
49. Davis, T. J. et al. Ultrafast vector imaging of plasmonic skyrmion dynamics with deep subwavelength resolution. *Science* **368**, 386–390 (2020).
50. Ghosh, A. et al. A topological lattice of plasmonic merons. *Appl. Phys. Rev.* **8**, 041413 (2021).
51. Dai, Y. et al. Ultrafast microscopy of a twisted plasmonic spin skyrmion. *Appl. Phys. Rev.* **9**, 011420 (2022).
52. Park, H. S. et al. Observation of the magnetic flux and three-dimensional structure of skyrmion lattices by electron holography. *Nat. Nanotechnol.* **9**, 337–342 (2014).
53. Roitman, D., Shiloh, R., Lu, P.-H., Dunin-Borkowski, R. E. & Arie, A. Shaping of electron beams using sculpted thin films. *ACS Photon.* **8**, 3394–3405 (2021).
54. Freimund, D. L., Aflatooni, K. & Batelaan, H. Observation of the Kapitza–Dirac effect. *Nature* **413**, 142–143 (2001).
55. Ostrovsky, E., Cohen, K., Tsesses, S., Gjonaj, B. & Bartal, G. Nanoscale control over optical singularities. *Optica* **5**, 283–288 (2018).
56. Walther, P. et al. Experimental one-way quantum computing. *Nature* **434**, 169–176 (2005).
57. Willig, K. I., Rizzoli, S. O., Westphal, V., Jahn, R. & Hell, S. W. STED microscopy reveals that synaptotagmin remains clustered after synaptic vesicle exocytosis. *Nature* **440**, 935–939 (2006).
58. Das, P. et al. Stimulated electron energy loss and gain in an electron microscope without a pulsed electron gun. *Ultramicroscopy* **203**, 44–51 (2019).
59. Ryabov, A., Thurner, J. W., Nabben, D., Tsarev, M. V. & Baum, P. Attosecond metrology in a continuous-beam transmission electron microscope. *Sci. Adv.* **6**, eabb1393 (2022).
60. Spektor, G. et al. Revealing the subfemtosecond dynamics of orbital angular momentum in nanoplasmonic vortices. *Science* **355**, 1187–1191 (2017).
61. Spektor, G. et al. Mixing the light spin with plasmon orbit by nonlinear light-matter interaction in gold. *Phys. Rev. X* **9**, 021031 (2019).
62. Dai, Y. et al. Plasmonic topological quasiparticle on the nanometre and femtosecond scales. *Nature* **588**, 616–619 (2020).

63. Prinz, E. et al. Functional meta lenses for compound plasmonic vortex field generation and control. *Nano Lett.* **21**, 3941–3946 (2021).
64. Dai, Y. et al. Ultrafast nanofemto photoemission electron microscopy of vectorial plasmonic fields. *MRS Bull.* **46**, 738–746 (2021).
65. Kozák, M., Schönenberger, N. & Hommelhoff, P. Ponderomotive generation and detection of attosecond free-electron pulse trains. *Phys. Rev. Lett.* **120**, 103203 (2018).
66. Cho, B., Ichimura, T., Shimizu, R. & Oshima, C. Quantitative evaluation of spatial coherence of the electron beam from low temperature field emitters. *Phys. Rev. Lett.* **92**, 246103 (2004).
67. Xiaoyan, L. et al. Three-dimensional vectorial imaging of surface phonon polaritons. *Science* **371**, 1364–1367 (2021).
68. Gordon, E. I. A review of acoustooptical deflection and modulation devices. *Appl. Opt.* **5**, 1629–1639 (1966).
69. Bernien, H. et al. Probing many-body dynamics on a 51-atom quantum simulator. *Nature* **551**, 579–584 (2017).
70. Gjonaj, B. et al. Active spatial control of plasmonic fields. *Nat. Photon.* **5**, 360–363 (2011).

Methods

Sample preparation

We coated a 40 nm layer of Au atop a 30 nm Si_3N_4 transmission electron miscroscopy membrane (Norcada, NTX025) using sputter deposition (AJA International, ATC 2200), with a 3 nm Ti adhesion layer. We use only the long-range SPP-guided wave in our set-up, which is localized at the sample boundaries and is only weakly affected by the adhesion layer (sample illustration and mode shape appear in Extended Data Fig. 1a). After fabrication of the Au-coated membrane, plasmonic coupling slits are milled into it using a focused ion beam (FEI, Helios NanoLab DualBeam G3 UC), etching only through the Au coating, leaving the Si_3N_4 layer intact. The plasmonic coupling slits were optimized for broadband operation around an excitation wavelength of 730 nm. A top view of the entire sample from the Au side is given in Extended Data Fig. 1b.

Experimental set-up

We performed the measurements using the experimental set-up described in ref. [31]. Laser pulses are frequency-quadrupled to induce photoemission of electron pulses from the tip source of the electron microscope. These electrons are then accelerated and impinge on a nanostructured membrane in sync with laser pulses that generate a plasmonic near field interacting with the electrons. Laser pulses impinging on the sample were tuned to a central wavelength of 730 nm by an optical parametric amplifier (Light Conversion, Orpheus), and their polarization was externally tunable via a broadband $\lambda/4$ plate.

For the experiments described in Figs. 2, 4 and 5c and the inset in Fig. 3a, we used laser pulses of ~220 fs (FWHM), at a 1 MHz repetition rate and with an energy of ~25 nJ (25 mW average power), while EFTEM was performed with an ~10-eV-wide slit centred at 6 eV at the gain side of the energy loss spectrometer, practically observing all electrons that gained energy in their interaction. For the experiment described in Fig. 5, the laser pulses were stretched using a 12 mm ZnSe window (Edmund Optics, Light Pipe) to ~840 fs (FWHM), and their energy was either ~30 nJ (30 mW average power) or 65 nJ (65 mW average power). EFTEM was performed with an ~1 eV slit, centred around multiples of the central laser pulse frequency (0 eV, −1.7 eV, −3.4 eV, −5.1 eV, −6.8 eV and −8.5), such that only electrons at a certain interaction order were imaged (with a small residual signal from other interaction orders). The electron diffraction in Fig. 3 was performed in the HD diffraction mode of the microscope (JOEL 2100+), with laser pulses similar to those in Fig. 5. Apertures of 20 µm (Fig. 3a) and 50 µm (Fig. 3f) in diameter, marked in the presented scanning electron microscopy (SEM) micrographs, were placed right after the sample. By considering the spot size of the diffracted electron in Fig. 3d, as well as taking into account the calibrated distances in the diffraction plane given by the manufacturer, we extract a conservative estimate for the electron transverse coherence length in this measurement of 1 µm.

Electron pulse width and energy width were ~350 fs and ~1.1 eV for all experiments, with negligible incoherent broadening from the transmission through the sample. The beam width used was varied according to the required magnification in each figure (as shown in the corresponding scale bars) except in Fig. 3, where the beam was expanded to an ~2 mm diameter before impinging on the sample. In Figs. 2 and 4, a fraction of ~30–50% out of all the electrons going through the sample is detected. In Fig. 5, the fraction of electrons per interaction order varies but is obviously lower (ideally, this number could increase to ~35% in the required interaction order, as shown theoretically in ref. [24]). Due to our electron source and electron optical system, only ~10% of the electrons emitted from the tip in our experiment end up going through the sample, a technical limitation that can be largely overcome, as in ref. [20]. The electron energy filtering scheme in each part of the experiment is illustrated in Extended Data Fig. 2 (note that energy filtering was not performed in Fig. 3).

The sample was tilted at an angle of ~4.5° to allow normal incidence of the laser pulses. Changes as small as 0.1° to this angle create aberrations in the shape of the spatially modulated electrons (in Supplementary Video 3, the sample tilt is varied between 4.1° and 4.9°), which provides another degree of freedom for controlling the electron wavefunction.

Theory of free-electron–light interaction

Our theoretical formalism is based on the one derived in ref. [30]. We describe the interaction of a free electron and an electromagnetic wave by using the time-dependent Schrödinger equation:

$$\left[\frac{(\mathbf{p}+e\mathbf{A})^2}{m}-eV\right]\psi=\mathrm{i}\hbar\frac{\partial\psi}{\partial t}$$

where $\mathbf{p}$ is the momentum operator of the electron; e is the elementary charge; m is the electron mass; $\mathbf{A}$ is the electromagnetic vector potential; V is the electromagnetic scalar potential; and ψ is the electron wavefunction.

We apply the same assumptions in solving the above-mentioned equation as in all other papers on ultrafast transmission electron microscopy[28,29]. In short, the electron is highly paraxial, such that its longitudinal and transverse dynamics are decoupled, and the entire transverse dynamics can be neglected. This allows us to introduce the relativistic correction to the equation by simply replacing $m \to \gamma m$ (where γ is the relativistic Lorentz factor). As a consequence of these conventional conditions, we can reach the form given in equation (1).

To solve equation (1), it is customary[32] to assume that the electron is made up of a carrier wave and a slowly varying envelope, which can be decomposed to harmonics of the frequency of the electromagnetic wave

$$\psi=\exp(\mathrm{i}\left(k_0 z-\frac{U_0}{\hbar}t\right))\phi_0(\mathbf{r}-v t\hat{z})\sum_l \exp(\mathrm{i}l\omega\left(\frac{z}{v}-t\right))f_l(\mathbf{r})$$

where U_0 and k_0 are the initial energy and momentum of the paraxial electron, respectively; $\hbar$ is the reduced Planck constant; ϕ_0 is a slowly varying envelope function; ω is the frequency of the electromagnetic wave; v is the initial electron velocity; $\mathbf{r}=(x,y,z)$ is the coordinate vector, with z being the longitudinal coordinate; and l and f_l are the interaction order and its spatially dependent coefficient, with negative orders denoting emission and positive orders denoting absorption.

When solving equation (1) with the above assumption for the wavefunction, one can extract an equation for the spatially dependent coefficient of each interaction order:

$$\frac{\partial f_l(\mathbf{r})}{\partial z}=\frac{e}{\hbar\omega}\left(E_z^*\exp(\mathrm{i}\omega\frac{z}{v})f_{l+1}(\mathbf{r})-E_z\exp(-\mathrm{i}\omega\frac{z}{v})f_{l-1}(\mathbf{r})\right).$$

This results in the final expression

$$f_l(\mathbf{r})=\exp(\mathrm{i}l\arg(-g(x,y)))J_l(2|g(x,y)|)$$

where $g(x,y)=\frac{e}{\hbar\omega}\int_{-\infty}^{\infty}E_z(x,y,z)\exp(-\mathrm{i}\frac{\omega}{v}z)\mathrm{d}z$ is the free-electron–light interaction strength; J_l is the lth order Bessel function of the first kind; and E_z is the electric field phasor in the direction of electron propagation (the out-of-plane direction of our sample). The longitudinal dependence of the SPP field in our system is given in Extended Data Fig. 1a, and a representative transverse distribution is given in Extended Data Fig. 3a,b.

Under the approximation that $g \ll 1$, the coefficients of all interaction orders are negligible except for the first, and thus the transverse distribution of electrons gaining energy in the interaction is $P_T \approx |f_1(x,y)|^2$, where $f_1(x,y) \approx 2|g(x,y)|\exp(\mathrm{i}\arg(-g(x,y)))$. Consequently, the transverse electron probability distribution follows the spatially

dependent intensity of the SPP field (Extended Data Fig. 3c,d). A similar scaling also appears for larger values of g, provided that the electron pulse duration is longer than the laser pulse duration. In this scenario, the free-electron–light interaction strength is time dependent, resulting in an average interaction strength that is, again, small. Both of these cases form the regime we refer to as the low-intensity regime, and the label of the high-intensity regime applies when they are no longer valid.

Image acquisition and processing

Images of the electron spatial distribution in Figs. 2 and 4 were acquired by a camera mounted on an EELS instrument (Gatan US1000), using an exposure time of 120 s per image. Images of the electron spatial distribution in Figs. 3a and 5 were acquired using a direct-detection camera (Gatan K2), with an exposure time of 480 s per image. Electron diffraction images in Fig. 3b–e (smaller aperture) were integrated for 16 hours with laser illumination and for 4 hours without it. Electron diffraction images in Fig. 3g–j (larger aperture) were integrated for 2.66 hours with laser illumination and for 0.66 hours without it. All images in Fig. 3 were taken with an increased camera pixel threshold to greatly reduce noise levels. The large beam diameter required for diffraction measurement in our experiment (preset in the microscope), coupled with the required aperture sizes following the sample, led to low signal levels in our diffraction images. This, however, is not a fundamental limit, and is directly connected to the quality of our electron source and optics, which may be vastly improved[20].

In all images, however, two main sources of noise exist: background noise and random flaring of detector pixels. As a result, the detector software usually performs substantial automated image processing on the raw image data. We exported the raw data (Extended Data Fig. 4a) and performed the image processing ourselves. Correcting the images for random pixel flaring requires contrast manipulation, which is performed by considering the distribution of the image histogram and choosing lower and upper bounds (Extended Data Fig. 4b). We chose the average pixel signal as the lower bound, while the upper bound was chosen to be the highest pixel value five standard deviations from the average (this number changes for each image). Background noise may be removed by equalization—reducing the average pixel value from each pixel. A representative result of the full image processing is given in Extended Data Fig. 4c, matched against the image produced by the detector software (Extended Data Fig. 4d).

The diffraction images are made up of several short exposure images that were superimposed using a centre-of-mass algorithm, correcting for drift due to the long measurement times, to achieve the raw data images appearing in Fig. 3. To reach the deconvolved images of Fig. 3, the following process was performed: the electron diffraction without laser illumination was interpolated, smoothed with a Gaussian filter and truncated to act as a deconvolution kernel for all other images. The same process was repeated for the other images, and deconvolution was performed with a standard commercial algorithm. A further contrast manipulation was made to ensure the visibility of weak diffraction peaks.

Data availability

Due to the large size of the raw data files (over 16.5 GB), the data supporting the findings of this study are available from the corresponding author upon reasonable request.

Acknowledgements

Samples were prepared at Technion's Micro and Nano Fabrication Unit, with the help of G. Ankonina and L. Popilevsky. Measurements were conducted in I.K.'s UTEM laboratory in the electron microscopy centre (MIKA) in the Department of Materials Science and Engineering of the Technion. We acknowledge the Russell Berrie Nanotechnology Institute and the Hellen Diller Quantum Center for their support of this research. S.T. acknowledges support by the Adams Fellowship Program of the Israel Academy of Science and Humanities and thanks A. Karnieli, A. Arie, Y. Kauffmann and M. Krueger for helpful conversations. R.D. thanks G. M. Vanacore for helpful discussions on performing electron diffraction. We are especially grateful to the Q-SORT consortium for inspiring this work. I.K. acknowledges the support of the Azrieli Faculty Fellowship. This research was supported by the European Research Council starting grant NanoEP 851780, the European Union's Horizon 2020 research and innovation programme grant SMART-electron 964591 and the Israel Science Foundation grants 3334/19 and 831/19.

Author contributions

S.T. and I.K. conceived the project. S.T. and K.C. designed and fabricated the samples. R.D., S.T. and K.W. conducted the measurements. O.R., S.T. and T.B. performed simulations and theoretical calculations. G.B. and I.K. supervised the project. All authors participated in writing the manuscript and analysing the experimental results.

Competing interests

The authors declare no competing interests.

Additional information

Extended data is available for this paper at https://doi.org/10.1038/s41563-022-01449-1.

Supplementary information The online version contains supplementary material available at https://doi.org/10.1038/s41563-022-01449-1.

Correspondence and requests for materials should be addressed to Ido Kaminer.

Peer review information *Nature Materials* thanks Benjamin McMorran and the other, anonymous, reviewer(s) for their contribution to the peer review of this work.

https://doi.org/10.1038/s41563-022-01449-1

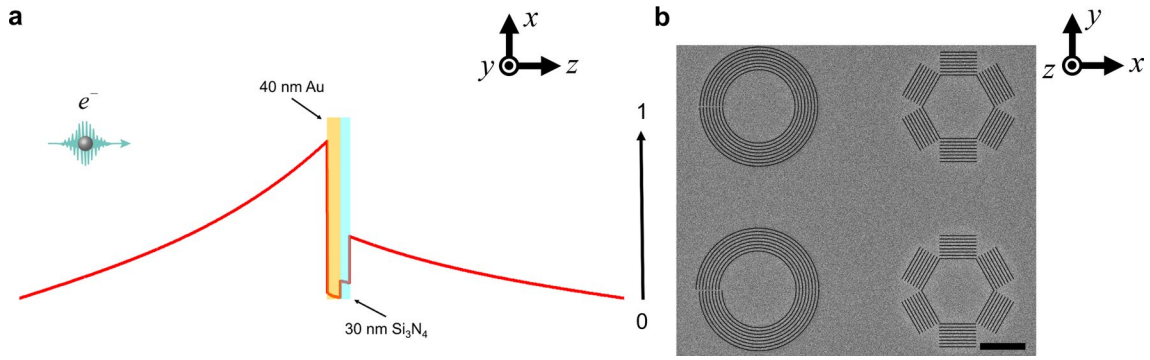

Extended Data Fig. 1 | Sample design and fabrication. (a) Illustration of the sample used in the experiments, overlaid with the cross-section of the long-range surface plasmon polariton (SPP), showing its electric field amplitude in the direction of electron propagation ($|E_z|$). The vertical arrow provides an axis for the SPP amplitude profile. **(b)** A SEM micrograph of the various plasmonic coupling slits used in our experiments, which were optimized for broadband operation around an excitation wavelength of 730 nm and milled into the gold layer of the sample (scale bar is 10 microns). The coordinate system of the experiment appears in both (a) and (b), rotated to fit the observation direction in each case.

https://doi.org/10.1038/s41563-022-01449-1

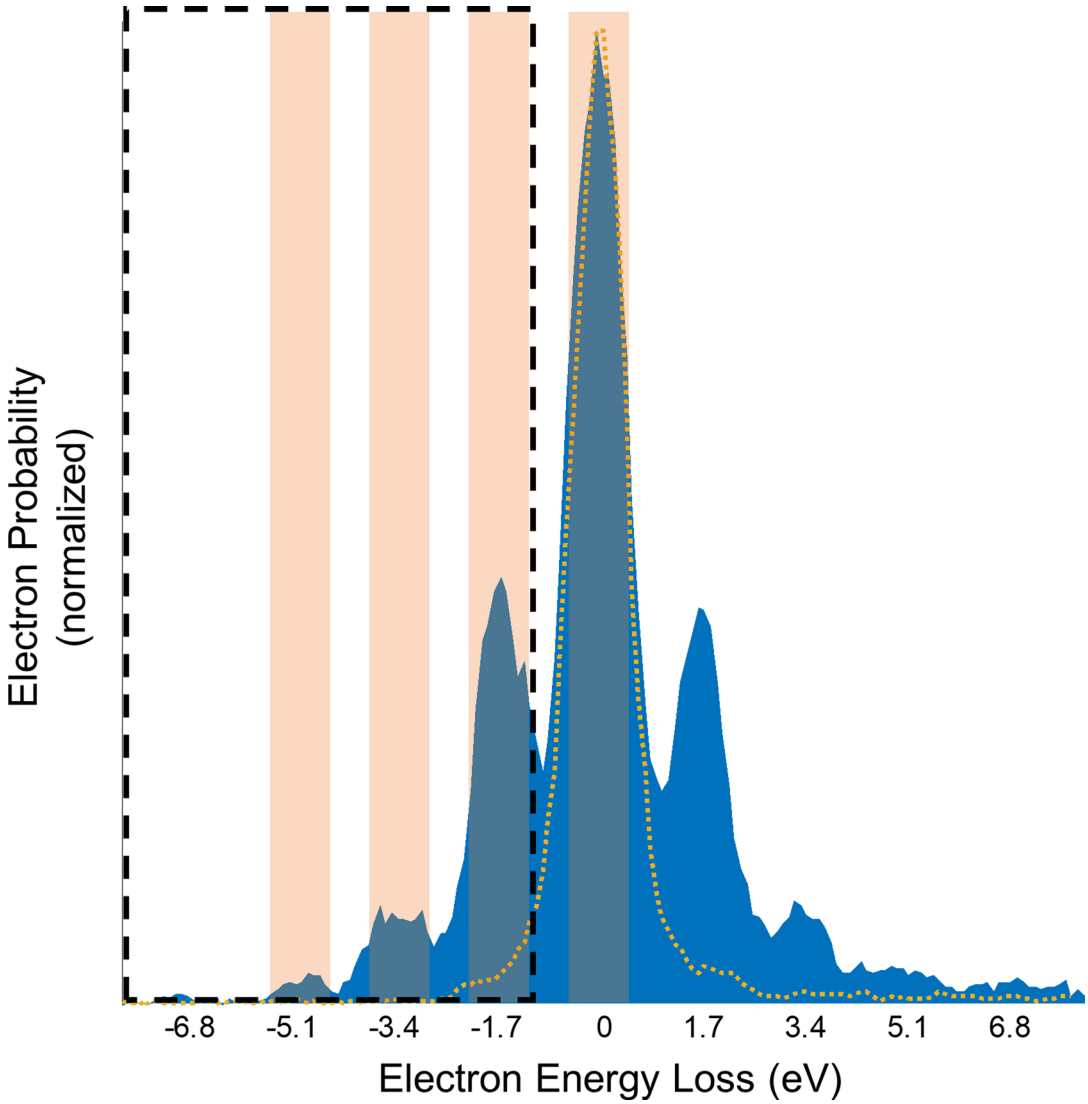

Extended Data Fig. 2 | Electron energy filtering schemes used in the experiment. The figure shows a representative measurement of the electron energy loss spectrum (EELS) measured in our experiment (blue area), with visible peaks at integer multiples of the laser pulse (~1.7 eV). The measured EELS without laser pulse excitation is given by the dotted gold curve. For the measurements performed in Figs. 2–3, we filter electrons that gained energy, as marked by the dashed black frame, effectively adding up all positive free-electron–light interaction orders. For the measurements performed in Fig. 4, we filter electrons that underwent interactions of specific orders, as marked by the light orange rectangles (each with a ~1 eV energy width). The energy dispersion of our EELS measurement was 0.1 eV per pixel.

https://doi.org/10.1038/s41563-022-01449-1

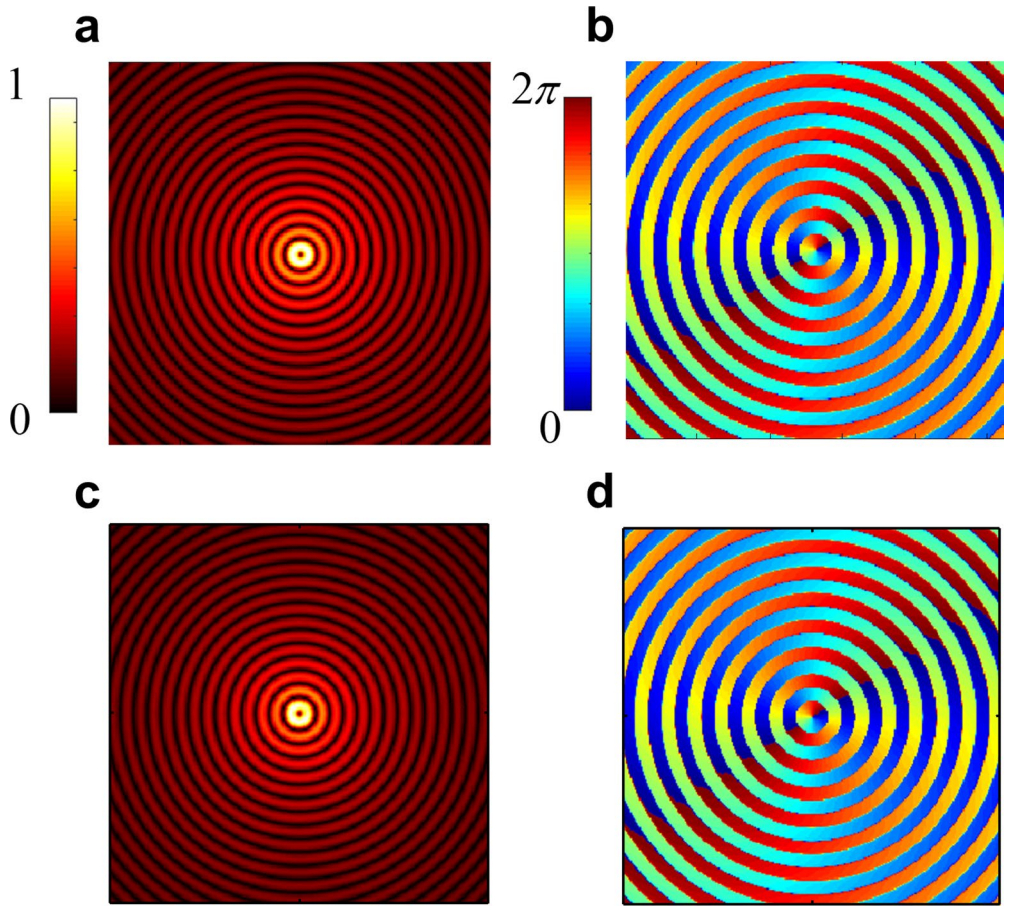

Extended Data Fig. 3 | Theory of photon-induced amplitude and phase modulation. (a),(b) Calculated amplitude and phase of the out-of-plane electric field for a 1st order plasmonic Bessel vortex, created by a circular coupling slit as in Fig. 2b. The field is calculated via the Huygens principle method. **(c),(d)** Calculated amplitude and phase of the transverse electron wavefunction, after interaction with the SPP vortex presented in (a),(b), in the low-intensity interaction regime. The wavefunction distribution is calculated via the expression given in Methods section, by summing over the first 10 interaction orders. The fine match between the electron and electric field distributions suggests that light shapes both the electron amplitude and phase, as was also verified by the diffraction measurement in Fig. 3. A specific consequence of shaping both the amplitude and the phase is that angular momentum can indeed be transferred from the SPP vortex field to the electrons interacting with it.

https://doi.org/10.1038/s41563-022-01449-1

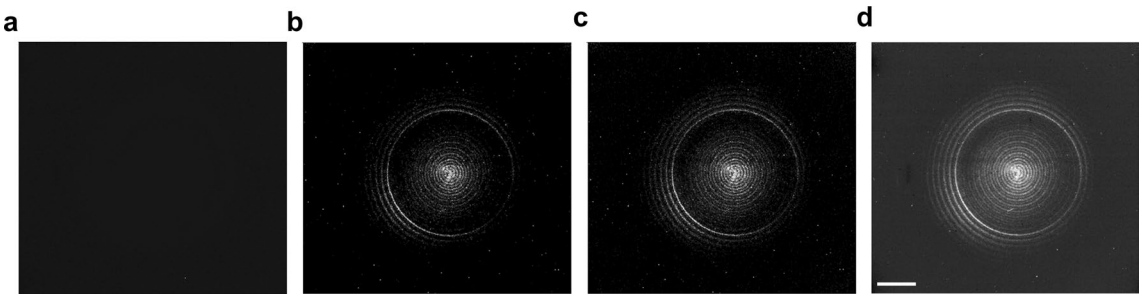

Extended Data Fig. 4 | Image processing of the electron distribution measurements. The figure illustrates the process of creating the electron distribution images presented throughout the manuscript. **(a)** The raw data without any manipulation. Random pixel flaring greatly reduces image contrast, making it seem as though there is no signal. **(b)** Mitigation of random pixel flaring by contrast manipulation, as described in Methods section. **(c)** Equalization of the image after contrast manipulation enables the visualization of more detailed features. **(d)** The image generated automatically from the detector software, qualitatively similar to the image that we extracted. The white scale bar in (d) is relevant for all images and corresponds to 5 microns.